Chaos, Solitons and Fractals 179 (2024) 114456

Contents lists available at ScienceDirect

Chaos, Solitons and Fractals

journal homepage: www.elsevier.com/locate/chaos

Stable semivortex gap solitons in a spin–orbit-coupled Fermi gas

P. Díaz [a,*], H. Molinares [a], L.M. Pérez [b], D. Laroze [c], J. Bragard [d], B.A. Malomed [e]

[a] Departamento de Ciencias Físicas, Universidad de La Frontera, Casilla 54-D, Temuco 4780000, Chile
[b] Departamento de Física, FACI, Universidad de Tarapacá, Casilla 7D, Arica 1000000, Chile
[c] Instituto de Alta Investigación, Universidad de Tarapacá, Casilla 7D, Arica 1000000, Chile
[d] Departamento de Física y Matemática Aplicada, Universidad de Navarra, 31080, Pamplona, Spain
[e] Department of Physical Electronics, School of Electrical Engineering, Faculty of Engineering, Tel Aviv University, Ramat Aviv, 69978, Israel

ARTICLE INFO

Keywords:
Fermi systems
Spin–orbit coupling
Semivortex solitons
Gap solitons
Soliton stability

ABSTRACT

We demonstrate the existence of semivortex (SV) solitons, with vorticities 0 and 1 in the two components, in a two-dimensional (2D) fermionic spinor system under the action of the Rashba-type spin–orbit coupling in the combination with the Zeeman splitting (ZS). In the "heavy-atom" approximation, which was previously elaborated for the bosonic system, the usual kinetic energy is neglected, which gives rise to a linear spectrum with a bandgap. The model includes the effective Pauli self-repulsion with power 7/3, as produced by the density-functional theory of Fermi superfluids. In the general case, the inter-component contact repulsion is included too. We construct a family of gap solitons of the SV type populating the spectral bandgap. A stability region is identified for the SV solitons, by means of systematic simulations, in the parameter plane of the cross-repulsion strength and chemical potential. The stability region agrees with the prediction of the anti-Vakhitov-Kolokolov criterion, which is a relevant necessary stability condition for systems with self-repulsive nonlinearities. We also test the stability of the SV solitons against a sudden change of the ZS strength, which initiates robust oscillations in the spin state of the soliton due to transfer of particles between the system's components.

1. Introduction

Since the first observation of the Bose–Einstein condensates (BECs) as a quantum state of matter in atom gases at temperatures of tens of nano-Kelvin in 1995 [1–3], the progress in this area of condensed-matter and atomic physics has been truly spectacular [4–11]. From the experimental point of view, the progress in the development of magneto-optical traps, optical lattices, and the control of interactions between particles [4,5,12–20] has led to great expansion of the variety of phenomena observed in this realm – in particular, due to the possibility of tuning the effective sign and strength of inter-atomic interactions. One of fast developing directions of the studies is the possibility to design various forms of the synthetic (pseudo-) spin–orbit coupling (SOC) between different atomic states, using appropriate modes of laser illumination [21,22]. While in most experimental works SOC was emulated in effectively one-dimensional (1D) BEC settings, its experimental realization in 2D was reported too [23].

The inclusion of SOC in the context of theoretical studies has opened the possibility of creating stable matter-wave solitons in 2D and 3D free space, without confining potentials [24–35]. Furthermore, gap solitons have been predicted by considering the interplay of SOC with the Zeeman splitting (ZS) between the components of the binary BECs [24,25,36,37].

The studies of quantum states of matter in ultracold Fermi gases have also demonstrated great advancement. In particular, realization of SOC in atomic Fermi systems has been reported [38,39]. Theoretically, a possibility of the existence of gap solitons, due to the interplay of the Pauli self-repulsion, induced by the atomic Fermi distribution, and a spatially-periodic potential imposed by an external optical lattice, has been predicted in the framework of the density-functional theory [40]. The existence of 2D solitons in a free-space binary fermionic cloud, under the action of SOC and attraction between the two components, has been demonstrated too [41], see Ref. [42] for a review.

In this work, by means of systematic numerical analysis, we report the existence and stability of 2D gap solitons of the semivortex (SV) type, i.e., ones with vorticities 0 and 1 in its two components, in the binary Fermi system carrying SOC of the Rashba type and ZS along with the Pauli self-repulsion produced by the density-functional approximation. To construct the SV solitons, we adjust the approach, which was previously elaborated for binary BEC in Ref. [36], to the fermionic system. Namely, assuming the presence of strong SOC

* Corresponding author.
E-mail address: pablo.diaz@ufrontera.cl (P. Díaz).

https://doi.org/10.1016/j.chaos.2024.114456
Received 7 December 2023; Accepted 3 January 2024
Available online 17 January 2024

and ZS terms, the usual kinetic energy is neglected, which gives rise to a bandgap in the system's spectrum, that may be populated by solitons.

The following presentation is structured as follows: in Section 2, we introduce the theoretical model and methodology. Section 3 demonstrates the existence of an SV soliton family populating the system's bandgap. In Section 4 we explore stability of the soliton solutions. Section 5 addresses oscillatory dynamics of the solitons initiated by a sudden change of the ZS coefficient. The paper is concluded by Section 6.

2. The model and methods

In the framework of the functional-density (mean-field) theory for the Fermi superfluid, which has been extensively elaborated in the literature [43–55], we consider the 2D spinor wave function,

$$\boldsymbol{\Phi}(x,y,t)=(\boldsymbol{\Phi}_{+}(x,y,t),\boldsymbol{\Phi}_{-}(x,y,t)),$$

whose spatiotemporal evolution is governed by the system of coupled of mean-field equations:

$$\begin{aligned} i\partial_t\boldsymbol{\Phi}_{+} &= +\lambda_R\left(\partial_x-i\partial_y\right)\boldsymbol{\Phi}_{-}+\Omega\boldsymbol{\Phi}_{+} \\ &\quad+\left(\left|\boldsymbol{\Phi}_{+}\right|^{4/3}-\gamma\left|\boldsymbol{\Phi}_{-}\right|^{2}\right)\boldsymbol{\Phi}_{+}, \end{aligned} \tag{1}$$

$$\begin{aligned} i\partial_t\boldsymbol{\Phi}_{-} &= -\lambda_R\left(\partial_x+i\partial_y\right)\boldsymbol{\Phi}_{+}-\Omega\boldsymbol{\Phi}_{-} \\ &\quad+\left(\left|\boldsymbol{\Phi}_{-}\right|^{4/3}-\gamma\left|\boldsymbol{\Phi}_{+}\right|^{2}\right)\boldsymbol{\Phi}_{-}, \end{aligned} \tag{2}$$

with terms $\left|\boldsymbol{\Phi}_{\pm}\right|^{4/3}\boldsymbol{\Phi}_{\pm}$ accounting for the Pauli self-repulsion in the framework of the density-functional theory, and cubic terms $-\gamma\left|\boldsymbol{\Phi}_{\mp}\right|^{2}\boldsymbol{\Phi}_{\pm}$ representing the contact interaction between the two components (positive and negative γ corresponds to the attractive and repulsive interactions, respectively). Further, λ_R is a real coefficient representing SOC of the Rashba type [56], which has been widely studied in this form for the binary BEC [22,24,26–28], and more recently for fermionic systems [41], while $\Omega>0$ is the ZS strength. Note that the scaling transformation makes it possible to fix $\lambda_R=\Omega\equiv 1$, which is adopted below.

Eqs. (1), (2) are derived from the underlying 3D system, assuming that the system is subject to strong confinement in the transverse direction, with the trapping scale a_z. The 2D model introduced here is appropriate for the consideration of localized structures with lateral size $l\gg a_z$. Furthermore, following Refs. [30,36], we here address the case in which the SOC and ZS terms are much larger than the kinetic-energy term (the limit of "heavy atoms"), therefore the usual Laplacians which represents the kinetic energy are dropped in Eqs. (1) and (2).

It is relevant to cast the system of Eqs. (1) and (2) in the Hamiltonian form:

$$\begin{aligned} &i\partial_t\boldsymbol{\Phi}_{\pm}=\frac{\delta H}{\delta\boldsymbol{\Phi}_{\pm}^{*}}, \\ &H=\iint dxdy\left\{\lambda_R\left[\boldsymbol{\Phi}_{+}^{*}\left(\partial_x-i\partial_y\right)\boldsymbol{\Phi}_{-}+\boldsymbol{\Phi}_{+}\left(\partial_x+i\partial_y\right)\boldsymbol{\Phi}_{-}^{*}\right]\right. \\ &\left.+\Omega\left(\left|\boldsymbol{\Phi}_{+}\right|^{2}-\left|\boldsymbol{\Phi}_{-}\right|^{2}\right)+\frac{3}{5}\left(\left|\boldsymbol{\Phi}_{+}\right|^{10/3}+\left|\boldsymbol{\Phi}_{-}\right|^{10/3}\right)-\gamma\left|\boldsymbol{\Phi}_{+}\right|^{2}\left|\boldsymbol{\Phi}_{-}\right|^{2}\right\}, \end{aligned} \tag{3}$$

where $*$ and $\delta/\delta\boldsymbol{\Phi}_{\pm}^{*}$ stand for the complex conjugate and variational derivative, respectively. Hamiltonian H and norm

$$N=2\pi\iint dxdy\left[\left|\phi_{+}(x,y)\right|^{2}+\left|\phi_{-}(x,y)\right|^{2}\right]\equiv N_{+}+N_{-} \tag{4}$$

(where $N_{\pm}$ are populations of components $\phi_{\pm}$ of the spinor wave function), are dynamical invariants of the system of Eqs. (1) and (2). The system also conserves the vectorial momentum, which is given by the usual expression,

$$\mathbf{P}=i\iint dxdy\left(\boldsymbol{\Phi}_{+}\nabla\boldsymbol{\Phi}_{+}^{*}+\boldsymbol{\Phi}_{-}\nabla\boldsymbol{\Phi}_{-}^{*}\right). \tag{5}$$

To establish the conserved angular momentum of the same system, one should rewrite Hamiltonian (3) for the spinor components $\boldsymbol{\Phi}_{-}$ and $\tilde{\boldsymbol{\Phi}}_{+}\equiv\exp\left(-i\theta\right)\boldsymbol{\Phi}_{+}$ in polar coordinates (r,θ):

$$\begin{aligned} H&=\int_0^{\infty}rdr\int_0^{2\pi}d\theta\left\{\lambda_R\left[\tilde{\boldsymbol{\Phi}}_{+}^{*}\left(\frac{\partial}{\partial r}-\frac{i}{r}\frac{\partial}{\partial\theta}\right)\boldsymbol{\Phi}_{-}+\tilde{\boldsymbol{\Phi}}_{+}\left(\frac{\partial}{\partial r}-\frac{i}{r}\frac{\partial}{\partial\theta}\right)\boldsymbol{\Phi}_{-}^{*}\right]\right. \\ &\left.+\Omega\left(\left|\tilde{\boldsymbol{\Phi}}_{+}\right|^{2}-\left|\boldsymbol{\Phi}_{-}\right|^{2}\right)+\frac{3}{5}\left(\left|\tilde{\boldsymbol{\Phi}}_{+}\right|^{10/3}+\left|\boldsymbol{\Phi}_{-}\right|^{10/3}\right)-\gamma\left|\tilde{\boldsymbol{\Phi}}_{+}\right|^{2}\left|\boldsymbol{\Phi}_{-}\right|^{2}\right\}. \end{aligned} \tag{6}$$

The invariance of this expression with respect to the arbitrary rotation in the (x,y) plane, $\theta\to\theta+\Delta\theta$, implies the conservation of the respective angular momentum, as defined by the Noether theorem [57]. It can be written, eventually, in terms of the original components $\boldsymbol{\Phi}_{\pm}$:

$$\begin{aligned} M&=i\int_0^{\infty}rdr\int_0^{2\pi}d\theta\left(\boldsymbol{\Phi}_{-}^{*}\frac{\partial}{\partial\theta}\boldsymbol{\Phi}_{-}+\tilde{\boldsymbol{\Phi}}_{+}^{*}\frac{\partial}{\partial\theta}\tilde{\boldsymbol{\Phi}}_{+}\right) \\ &\equiv\int_0^{\infty}rdr\int_0^{2\pi}d\theta\left[i\left(\boldsymbol{\Phi}_{-}^{*}\frac{\partial}{\partial\theta}\boldsymbol{\Phi}_{-}+\boldsymbol{\Phi}_{+}^{*}\frac{\partial}{\partial\theta}\boldsymbol{\Phi}_{+}\right)+\left|\boldsymbol{\Phi}_{+}\right|^{2}\right]. \end{aligned} \tag{7}$$

We have checked that all numerical simulations reported below conserve the total norm and angular momentum of the spinor system.

To define SV soliton solutions, we follow the lines of the analysis developed in the context of the mean-field theory for the spin–orbit-coupled BEC in Ref. [36]. To this end, we introduce an ansatz based on the separation of variables in the polar coordinates (r,θ), with integer vorticities

$$m_{-},m_{+}=m_{-}-1 \tag{8}$$

of the two components of the spinor wave function:

$$\boldsymbol{\Phi}_{\pm}(r,\theta,t)=e^{-i\mu t}e^{im_{\pm}\theta}\phi_{\pm}(r), \tag{9}$$

where real μ is the chemical potential, and $\phi_{\pm}(r)$ are real functions. The relation between m_{+} and m_{-} adopted in Eq. (8) is imposed by the form of the Rashba SOC terms in Eqs. (1) and (2), cf. Ref. [26]. Accordingly, the angular momentum (7) for ansatz (9) is $M_{m_{-}}=\left(1-m_{-}\right)N_{-}+\left(2-m_{-}\right)N_{+}$.

Substituting the ansatz, defined by Eqs. (8) and (9), in Eqs. (1) and (2), we arrive at the following equations for the radial functions:

$$\begin{aligned} \frac{d}{dr}\phi_{-} &= \mu\phi_{+}-\phi_{+}-\frac{m_{-}}{r}\phi_{-} \\ &\quad-\left(\phi_{+}^{4/3}-\gamma\phi_{-}^{2}\right)\phi_{+}, \end{aligned} \tag{10}$$

$$\begin{aligned} \frac{d}{dr}\phi_{+} &= -\mu\phi_{-}-\phi_{-}+\frac{m_{+}}{r}\phi_{+} \\ &\quad+\left(\phi_{-}^{4/3}-\gamma\phi_{+}^{2}\right)\phi_{-}, \end{aligned} \tag{11}$$

where, as said above, $\lambda_R=\Omega=1$ is fixed by means of scaling, the remaining free parameters being γ and μ. The family of SV solitons is characterized by the dependence of norm (4) on μ, see below.

Following Ref. [36], we are interested in finding SV gap solitons in the fundamental (ground) state, which corresponds to $m_{-}=0$ or $m_{+}=0$, while excited states, with $m_{-}\cdot m_{+}\neq 0$, are expected to be unstable. Thus, setting $m_{-}=0$ and $m_{+}=-1$, in agreement with Eq. (8), Eqs. (10) and (11) reduce to

$$\begin{aligned} \frac{d}{dr}\phi_{-} &= \mu\phi_{+}-\phi_{+} \\ &\quad-\left(\phi_{+}^{4/3}-\gamma\phi_{-}^{2}\right)\phi_{+}, \end{aligned} \tag{12}$$

$$\begin{aligned} \frac{d}{dr}\phi_{+} &= -\mu\phi_{-}-\phi_{-}-\frac{\lambda_R}{r}\phi_{+} \\ &\quad+\left(\phi_{-}^{4/3}-\gamma\phi_{+}^{2}\right)\phi_{-}. \end{aligned} \tag{13}$$

An alternative option is to set $m_{+}=0$, $m_{-}=+1$, and $\Omega=-1$, which corresponds to the ground-state SV which is a mirror image of the one corresponding to Eqs. (12) and (13).

For exponentially localized soliton solutions, Eqs. (12) and (13) take the linearized asymptotic form of at $r\to\infty$. It is easy to see that the respective system of two linear first-order equations can be reduced to

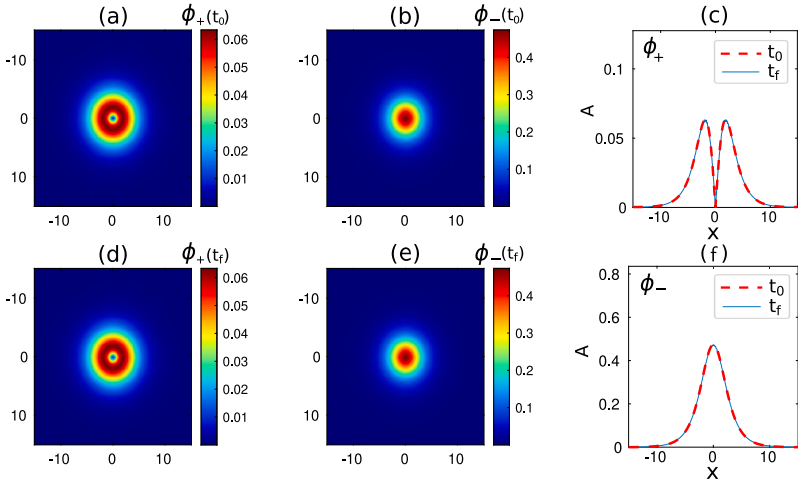

Fig. 1. Contour plots of the vortical and fundamental (zero-vorticity) components of the stable SV soliton, $|\Phi_+(x,y)|$ and $|\Phi_-(x,y)|$, respectively, in the (x,y) plane. (a,b) The input (at $t_0 = 0$), produced by the numerical solution of Eqs. (12) and (13). (d,e) The result produced by the evolution of the input (simulations of Eqs. (1) and (2)) at $t_f = 1000$. To verify the soliton's stability, the initial and final shapes of cross-sections of its vortical and fundamental components are compared, respectively. In panels (c) and (f). Parameters are $\gamma = 0$ (no nonlinear interaction between the components), $\lambda_R = 1$, $\Omega = 1$, $m_+ = -1$, $m_- = 0$, and $\mu = -0.88$. Note that this value of μ belongs to the corresponding bandgap (16). (For interpretation of the references to color in this figure legend, the reader is referred to the web version of this article.)

a single equation for $\phi_+(r)$, which is tantamount to the equation for the Bessel functions:

$$\frac{d^2\phi_+}{dr^2} + \frac{1}{r}\frac{d\phi_+}{dr} - \left(\frac{\Omega^2-\mu^2}{\lambda_R^2} + \frac{1}{r^2}\right)\phi_+ = 0, \tag{14}$$

the asymptotic expression for $\phi_-(r)$ being

$$\phi_-(r) = -\frac{\lambda_R}{\Omega+\mu}\left(\frac{d}{dr} + \frac{1}{r}\right)\phi_+(r). \tag{15}$$

As it follows from Eq. (14), the localized solutions may exist in the spectral *bandgap*, which is essentially the same as in the similar BEC system [36],

$$-\Omega < \mu < +\Omega. \tag{16}$$

Accordingly, the localized modes populating the bandgap are called gap solitons, as said above. At $r \to \infty$, their asymptotic form is given by the appropriate solution of Eq. (14),

$$\phi_+(r) = \phi_0^{(+)} K_1\left(\frac{\sqrt{\Omega^2-\mu^2}}{\lambda} r\right), \tag{17}$$

where K_1 is the modified Bessel function of the second kind, which exponentially decays $\sim r^{-1/2}\exp\left(-\frac{\sqrt{\Omega^2-\mu^2}}{\lambda} r\right)$, and $\phi_0^{(+)}$ is an arbitrary constant.

An asymptotic expansion of the relevant solution to Eqs. (12) and (13) can also be constructed at $r \to 0$:

$$\begin{aligned}
\phi_+(r) &= -\frac{\Omega+\mu}{\lambda_R}\phi_0^{(-)}\left(1 - \frac{\left(\phi_0^{(-)}\right)^{4/3}}{\Omega+\mu}\right) r + \mathcal{O}\left(r^3\right), \\
\phi_-(r) &= \phi_0^{(-)} + \frac{\Omega^2-\mu^2}{2\lambda^2}\phi_0^{(-)}\left(1 - \frac{\left(\phi_0^{(-)}\right)^{4/3}}{\Omega+\mu}\right) r^2 + \mathcal{O}\left(r^4\right),
\end{aligned} \tag{18}$$

where $\phi_0^{(-)}$ is another arbitrary constant.

Before producing systematic results for families of SV solitons, we display a generic example of a stable one in Fig. 1. Note that the chemical potential corresponding to this solution, $\mu = -0.88$, indeed belongs to bandgap (16).

3. Semivortex gap solitons

In this section, we summarize results for the SV gap solitons produced by the numerical solution of radial Eqs. (12) and (13). They were solved in the region of $0 \le r \le 30$, with the spatial mesh size $\Delta r = 10^{-5}$, by means of the shooting method together with the Euler method employed for the integration [58]. The boundary conditions at $r = 0$ were taken as $\phi_+(r=0) = 0$ and

$$\phi_-(r=0) = A > 0. \tag{19}$$

In the framework of this scheme, we looked for a value of A in Eq. (19) for which both fields tend to zero at $r \to \infty$ (in fact, this means $\phi_\pm(r = 30) = 0$ in the present setting), to build localized solutions. Several localized solutions, with different values of the norm (4), were thus found for increasing values of A. We selected the solution with the lowest value of N, which corresponds to the lowest A, as fundamental soliton. Higher-order ones, with greater A and greater N, correspond to excited localized states, which are expected to be completely unstable, as suggested by Ref. [36], where this conclusion was made in the context of the binary (spin–orbit-coupled) BEC model.

Fig. 2 summarizes our findings by means of heat maps exhibiting values of the amplitude (19), along with the total norm N and component populations $N_\pm$ (see Eq. (4)), in the plane of free parameters (γ, μ) of the system of Eqs. (12) and (13), in the ranges of $\gamma \in [-0.5, 0]$ and $\mu \in [-0.9, +0.9]$. We display the results only for $\gamma \le 0$, as the case of $\gamma > 0$, i.e., attraction between the components of the spinor wave function, leads to instability driven by the collapse. Indeed, a simple estimate following the lines of the general collapse theory [59] demonstrates that, in the 2D system with the dispersion represented by the first-order spatial derivatives, the critical or supercritical collapse occurs, respectively, under the action of a quadratic attractive nonlinearity, or any nonlinearity stronger than quadratic, including the cubic terms corresponding to $\gamma > 0$ in Eqs. (1) and (2).

Fig. 2(a) demonstrates that amplitude A notably increases with the increase of chemical potential μ, slightly decreasing with the increase of the negative cross-interaction coefficient γ. In panel (b), the total norm N increases with the increase of μ at a fixed value of γ, until it reaches a maximum value at points belonging to the curve labeled $N_{\max}$ in panel (b). The location of this line plays a key role in the discussion of the soliton stability below. Naturally, the maximum value of N increases for a less repulsive cross-interaction, i.e., smaller values of $(|\gamma|)$, allowing for the existence of more massive solitons. Panels

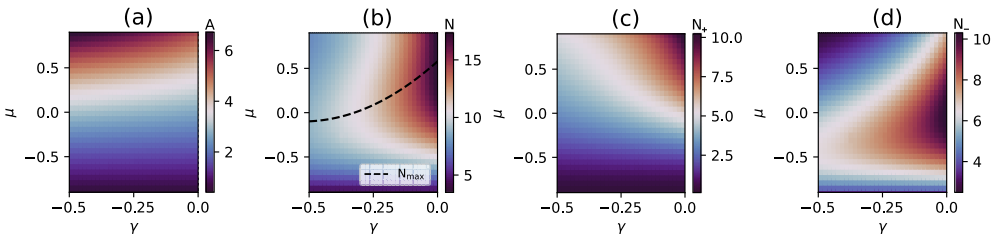

Fig. 2. (a) The heat map for amplitude (19) in the plane of the chemical potential μ and cross-interaction coefficient γ. Panels (b) and (c,d) display the same for the total norm N and populations of the two components, see Eq. (4).

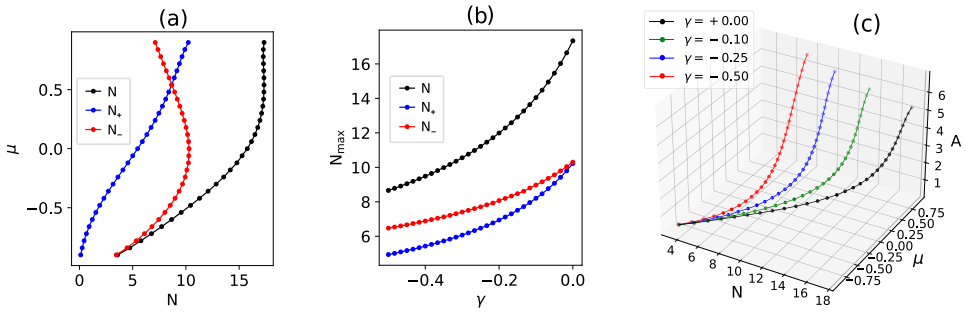

Fig. 3. (a) Curves $\mu(N)$, $\mu(N_+)$ and $\mu(N_-)$ for the family of SV solitons at $\gamma = 0$. (b) The largest values of the norm total and component norms from panels (b)–(d) of Fig. 2. (c) Amplitude A (see Eq. (19)) vs. the total norm N and chemical potential μ for different values of the cross-repulsion coefficient γ.

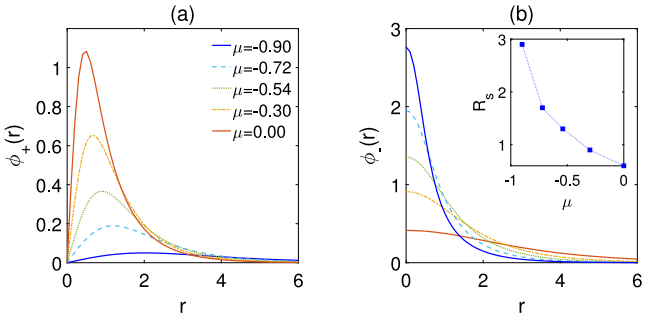

Fig. 4. Radial profiles of the vortical component ϕ_+ (a) and zero-vorticity one ϕ_- (b) for fixed $\gamma = -0.25$.

(c) and (d) demonstrate that the zero-vorticity spinor component (ψ_-) dominates at $\mu < 0$, while at $\mu > 0$ the norms of both components take close values, especially for smaller values of $|\gamma|$.

For further visualization of the findings, in Fig. 3(a) we present the relation between the chemical potential μ and the total norm N, along with the populations of the two components, for $\gamma = 0$. In particular, the two populations are equal for $\mu \approx 0.5$. The population distribution minimizing the Zeeman energy, i.e., having $N_- > N_+$ and thus helping to stabilize the SV solitons, is chosen by the system at $\mu < 0.5$. The distribution is inverted at $\mu > 0.5$, leading to the increase of the Zeeman energy and thus destabilizing the solitons, as shown below.

As demonstrated above in Fig. 2(b), the total norm attains a maximum value, $N_{\max}$, at a particular value of μ. The dependence of $N_{\max}$ on the inter-component repulsion coefficient γ is plotted in Fig. 3(b). This figure shows that, naturally, $N_{\max}$ decreases as the cross repulsion becomes stronger. Additionally, in this range of values of γ, the norm is predominantly concentrated in the zero-vorticity spinor without vorticity (Φ_-) which, as said above, helps to stabilize the SV solitons by reducing its Zeeman energy. Further, the dependence of the soliton's amplitude A on the norm N and, simultaneously, on the chemical potential μ (recall that μ is not an independent variable, but a function of N, pursuant to Fig. 3 (c)) is plotted in Fig. 3(c), for several different values of γ.

Radial profiles of the vortical and zero-vorticity components of the SV solitons, ϕ_+ and ϕ_- (see Eq. (9)), are presented in Fig. 4 for five different values of μ and fixed $\gamma = -0.25$. We observe that, in agreement with Fig. 2(a), the solitons increase their amplitude and become narrower with the increase of μ towards positive values. The inset in Fig. 4(b) shows the effective radius R_s of the soliton, which we define as the values of r at which the local value of the zero-vorticity component, $\phi_-(r)$, falls to 0.5 of $A \equiv \phi_-(r = 0)$ (see Eq. (19)). These results demonstrate that the matter density in the solitons steeply increases with the chemical potential. As shown in the next section, this trend leads to the onset of instability of the SV solitons.

4. Stability of the semivortex solitons

The above analysis suggests that variation of the cross-repulsion coefficient γ impacts on characteristics and shapes of the SV solitons, therefore one may expect that it also affects their stability. To address this issue, we have studied the stability of the soliton solutions in the parametric space (γ, μ) by means of direct simulation of Eqs. (1) and (2), taking, as the input, the ansatz (9) with the radial wave functions produced by the numerical solution of Eqs. (12) and (13). The simulations were performed by means of the fourth-order Runge–Kutta 4 method, with a fixed time-marching step $\Delta t = 10^{-4}$. Spatial derivatives were approximated using the standard centered second-order finite-difference scheme, with mesh sizes $\Delta x = \Delta y = 0.025$.

An example of an unstable SV soliton is presented in Fig. 5 for parameters $\gamma = 0$ and $\mu = -0.44$ (different from the example of the stable soliton presented above in Fig. 1, which pertains to $\mu = -0.88$). As seen in Fig. 5(d) and (e), the soliton's instability is evident at time $t = 160$. Panels (c) and (f) display the comparison of the initial soliton's profiles and ones produced by the evolution at $t = 160$ (blue and red curves, respectively). The examples presented in Figs. 1 and 5 reveal that the stability of the solitons strongly depends on values of the parameters, such as the chemical potential μ.

In the case of a dominant attractive nonlinearity, the necessary stability condition for solitons is given by the well-known Vakhitov-Kolokolov (VK) criterion, $d\mu/dN < 0$ [36,59,60]. In the present case, the Pauli repulsion term provides the dominant nonlinearity. As mentioned above, Eqs. (12) and (13) are similar to those addressed

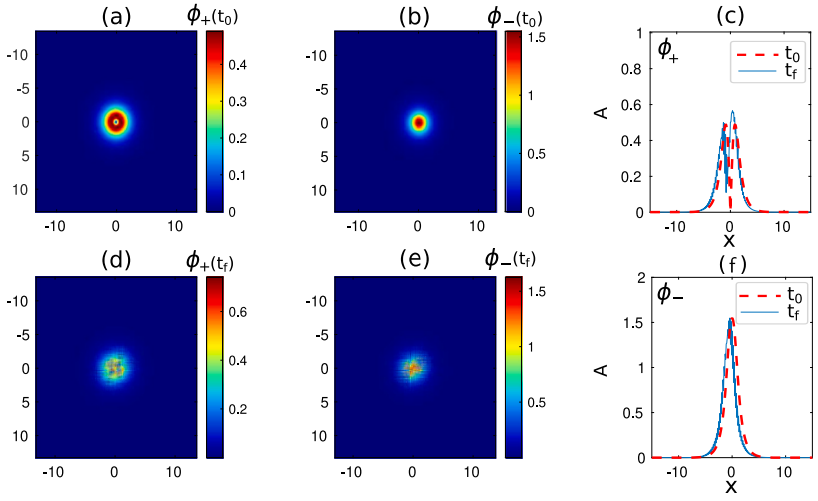

Fig. 5. An example of the unstable evolution of an SV soliton with $\gamma = 0$ and $\mu = -0.44$, produced by simulations of Eqs. (1) and (2). (a,b) Contour plots of the vortical and zero-vorticity components, $|\phi_+(r)|$ and $|\phi_-(r)|$, in the input. (d,e) The same at time $t_f = 160$. (c,f) Comparison of the initial and final profiles of the two components. (For interpretation of the references to color in this figure legend, the reader is referred to the web version of this article.)

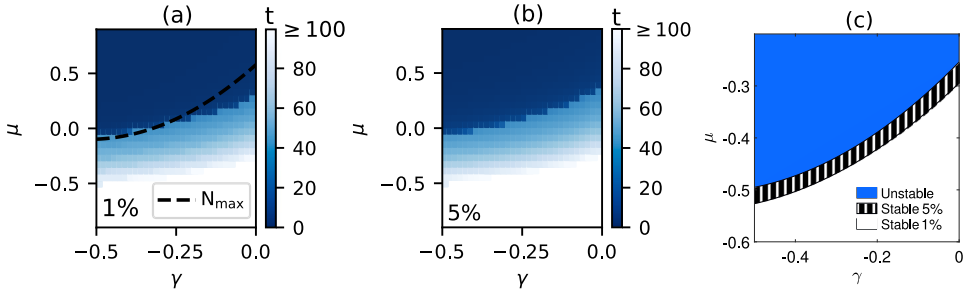

Fig. 6. The lifetime of the SV solitons as a function of the chemical potential μ and the cross-repulsion coefficient γ. Panels (a) and (b) display heat maps of the time at which the amplitude variation reaches the levels of 1% and 5%, respectively. (c) A sharper visualization of the regions where the same variations occur at $t \geq 100$ (for the stable solitons at sufficiently negative μ, the variations never take place).

in the context of the BEC gap-soliton model in Ref. [36], in which, however, the interaction was attractive. It is known that, in the case of the dominant repulsive nonlinearity, the VK stability criterion is replaced by the *anti-VK* one, *viz.*, $d\mu/dN > 0$ [61,62].

The stability of the SV-soliton family was tested by dint of the following procedure: the evolution of the amplitude at the center of the soliton, $|\Phi_-(x = y = 0, t)|$, was monitored, to record the time at which the amplitude deviates by 1% and 5% from the initial value, as shown in Fig. 6(a) and (b), respectively. Note that there is no significant difference between the figures. This means that, once the system is destabilized, attaining the amplitude variation of 1%, the variation of 5% was reached soon afterwards. The small difference between the times corresponding to 1% and 5% suggests that the 1% criterion is a sound indicator of the soliton stability. Next, we note that, for all values of γ, there is a value of μ for which the instability time is vanishingly small (indicating strong instability in the darkest regions of the maps). This critical value of μ becomes larger as γ approaches zero. Something similar happens in the opposite limit, which corresponds to the transition to stability: when the time necessary for the onset of the relative variation in the size of 1% exceeds $t = 100$ (the lighter region of the maps).

Fig. 6(c) displays the effective stability boundaries, displaying the lines below which the solitons remain stable according to the 5% and 1% criteria at $t \geq 100$. Returning to the parameter area in which the soliton's survival time tends to zero (the dark zone in Fig. 6(a,b)), it is seen, comparing it with Fig. 2(b), that the edge of this area coincides, approximately, with the curve at which N attains the maximum, as a function of μ, for each fixed value of γ (as indicated by the dashed line in Fig. 2(b)).

Note that, as Fig. 3(a) demonstrates (at least, for $\gamma = 0$), the anti-VK criterion, $d\mu/dN > 0$, definitely holds in the stability areas which are identified in Fig. 6, while the instability is correlated with the region in which this criterion becomes indefinite (corresponding to $dN/d\mu \approx 0$). Furthermore, if the same criterion is (tentatively) applied to the norm N_- of the dominating (zero-vorticity) component in Fig. 3(a), the point of transition from $d\mu/dN_- > 0$ to the (presumably) unstable region with $d\mu/dN_- < 0$ accurately predicts, for $\gamma = 0$, the actual stability boundary observed in Fig. 6. More detailed analysis of this issue, to be based on computation of eigenvalue spectra for eigenmodes of small perturbations, will be a subject of a separate work.

5. Oscillations

In this section, we address oscillatory dynamics of stable SV solitons. We start the analysis with a soliton taken in the stability zone ($\gamma = 0$, $\mu = -0.80$). The oscillations are initiated by a sudden change of the value of the Zeeman parameter, from $\Omega = 1$ fixed above to $\tilde{\Omega} = 1 + \Delta\Omega$ (the added detuning may be both positive and negative, $\Delta\Omega \gtrless 0$). The simulations were carried out up to time $t = 1000$. Fig. 7(a) shows the basic frequency of the internal oscillations in the solitons excited by this sudden perturbation, as a function of detuning $\Delta\Omega$.

To analyze the excited oscillations, we recorded the largest amplitude of the dominant zero-vorticity component of spinor wave function, thus creating a respective time series, $\left(A_-\right)_{\max}(t)$. Next, by applying the Fourier transform, we extract the basic frequency of the signals. Fig. 7(a) demonstrated a nearly linear dependence of the basic frequency on the detuning, in the considered range of $\Delta\Omega$ (the inset in

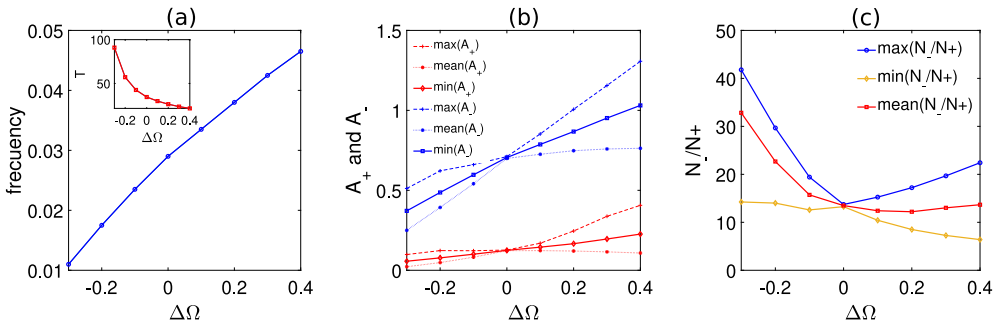

Fig. 7. (a) The frequency of the internal oscillations of the soliton, excited by the sudden change $\Delta\Omega$ of the ZS strength, vs. $\Delta\Omega$. (b) Amplitudes $A_+(t)$ and $A_-(t)$ as functions of $\Delta\Omega$. (c) The relative weight of the spinor components, $N_-/N_+(t)$, as a function of $\Delta\Omega$. Other parameters are $\gamma = 0$, $\mu = -0.8$, $\lambda_R = 1$, $\Omega = 1$, $m_+ = -1$, $m_- = 0$.

the figure displays the same result in terms of the dependence of the corresponding oscillation period on $\Delta\Omega$). Further, Fig. 7(b) displays the computed largest, smallest, and average values of the amplitudes of the vortical and zero-vorticity components, $A_+(t)$ and $A_-(t)$, vs. $\Delta\Omega$. Note that the difference between the largest and smallest values increases with $\Delta\Omega$, being greater when $\Delta\Omega > 0$. For both components, the average values increase monotonously, indicating that the SV become narrower and taller with the increase of Ω.

To complete the analysis, we consider the time series of the $N_-(t)/N_+(t)$ ratio, which is a record of the relative weight of the components. Fig. 7(c) shows that the highest average value of N_-/N_+ is reached at the most negative detuning considered, *viz.*, $\Delta\Omega = -0.3$, whereas it decreases and stabilizes at $\Delta\Omega > 0$. This fact demonstrates that the decrease in Ω (which leads to the contraction of the bandgap (16) populated by the gap solitons) favors the zero-vorticity component. Furthermore, Fig. 7(c) confirms that the internal oscillations of the soliton include the transfer of atoms between the two spin states. Thus, we infer that the stable SV solitons remain robust self-trapped modes even in the strongly excited state.

6. Conclusion

In the present work, we have shown the existence of semivortex solitons in the 2D fermionic spinor field, which includes the Rashba-type spin–orbit coupling and ZS (Zeeman splitting) between the two components, but does not include the usual kinetic energy (the approximation of "heavy atoms"). The spectrum of the system features a bandgap, which may be populated by gap solitons. The dominant nonlinearity in the system is provided by the Pauli repulsion, with power 7/3, as produced by the known density-functional approximation; the cubic repulsive interaction between the components is included too, in the general case. We have constructed a family of gap solitons of the SV (semivortex) type, with vortical and zero-vorticity components in the components with higher and lower Zeeman energies, respectively. The stability of the SV soliton family has been identified by means of systematic simulations of the perturbed evolution. The so identified stability region agrees with the known anti-Vakhitov-Kolokolov criterion. We have also investigated internal oscillatory dynamics of SV solitons initiated by a sudden change of the ZS coefficient. The stable solitons feature robust internal oscillations.

As an extension of the analysis, it is relevant to study the form and stability of moving SV solitons. This problem is nontrivial, as the underlying system of Eqs. (1) and (2) has no Galilean invariance. It is known that, if the equations are rewritten in the reference frame moving with speed c, the bandgap (16) shrinks to $\mu^2 < \sqrt{1-c^2}\Omega^2$ [36]. Once stable moving solitons can be found, it may also be interesting to simulate collisions between ones traveling with opposite speeds $\pm c$.

CRediT authorship contribution statement

P. Díaz: Conceptualization, Data curation, Formal analysis, Funding acquisition, Investigation, Methodology, Project administration, Resources, Software, Supervision, Validation, Visualization, Writing – original draft, Writing – review & editing. **H. Molinares:** Formal analysis, Investigation, Methodology, Visualization, Writing – original draft, Writing – review & editing. **L.M. Pérez:** Formal analysis, Investigation, Methodology, Software, Visualization, Writing – original draft, Funding acquisition. **D. Laroze:** Conceptualization, Formal analysis, Funding acquisition, Methodology, Resources, Supervision, Validation, Writing – original draft, Writing – review & editing. **J. Bragard:** Conceptualization, Formal analysis, Supervision, Validation, Writing – review & editing. **B.A. Malomed:** Conceptualization, Formal analysis, Methodology, Supervision, Validation, Writing – original draft, Writing – review & editing.

Declaration of competing interest

The authors declare that they have no known competing financial interests or personal relationships that could have appeared to influence the work reported in this paper.

Data availability

Data will be made available on request.

Acknowledgments

PD, LMP, and DL acknowledge partial financial support from FONDECYT 1231020. JB receives partial financial support through the project with reference: PID2020-116927RB-C22 of the Ministry of Economy and Competitivity (Spain). The work of BAM is supported, in part, by grant No. 1695/22 from the Israel Science Foundation. LMP acknowledges partial financial support from ANID through Convocatoria Nacional Subvención a Instalación en la Academia Convocatoria Año 2021, Grant SA77210040.

References

[1] Anderson MH, Ensher JR, Matthews MR, Wieman CE, Cornell EA. Observation of Bose-Einstein condensation in a dilute atomic vapor. Science 1995;269(5221):198–201.
[2] Davis KB, Mewes MO, Andrews MR, van Druten NJ, Durfee DS, Kurn DM, Ketterle W. Bose-Einstein condensation in a gas of sodium atoms. Phys Rev Lett 1995;75:3969–73.
[3] Bradley CC, Sackett CA, Tollett JJ, Hulet RG. Evidence of Bose-Einstein condensation in an atomic gas with attractive interactions. Phys Rev Lett 1995;75:1687–90.
[4] Bloch I, Dalibard J, Zwerger W. Many-body physics with ultracold gases. Rev Modern Phys 2008;80:885–964.

[5] Giorgini S, Pitaevskii LP, Stringari S. Theory of ultracold atomic Fermi gases. Rev Modern Phys 2008;80:1215–74.
[6] Yukalov VI. Difference in Bose-Einstein condensation of conserved and unconserved particles. Laser Phys 2012;22(7):1145–68.
[7] Dalibard J, Gerbier F, Juzeliūnas G, Öhberg P. Colloquium: Artificial gauge potentials for neutral atoms. Rev Modern Phys 2011;83:1523–43.
[8] Hauke P, Cucchietti FM, Tagliacozzo L, Deutsch I, Lewenstein M. Can one trust quantum simulators? Rep Progr Phys 2012;75(8):082401.
[9] Bloch I, Dalibard J, Nascimbène S. Quantum simulations with ultracold quantum gases. 2012;8(4):267276.
[10] Zhai H. spin-orbit coupled quantum gases. Internat J Modern Phys B 2012;26(1):12300010.
[11] Zhou X, Li Y, Cai Z, Wu C. Unconventional states of bosons with the synthetic spin–orbit coupling. J Phys B: At Mol Opt Phys 2013;46(13):134001.
[12] Baumann K, Guerlin C, Brennecke F, Esslinger T. icke quantum phase transition with a superfluid gas in an optical cavity. Nature 2010;464(7293):1301–6.
[13] Zipkes C, Ratschbacher L, Palzer S, Sias C, Köhl M. Hybrid quantum systems of atoms and ions. J Phys Conf Ser 2011;264(1):012019.
[14] Perron JK, Kimball MO, Mooney KP, Gasparini FM. Coupling and proximity effects in the superfluid transition in 4He dots. Nat Phys 2010;6(7):499502.
[15] Best T, Will S, Schneider U, Hackermüller L, van Oosten D, Bloch I, Lühmann D-S. Role of interactions in ^{87}Rb–^{40}K Bose-Fermi mixtures in a 3D optical lattice. Phys Rev Lett 2009;102:030408.
[16] Cumby TD, Shewmon RA, Hu M-G, Perreault JD, Jin DS. Feshbach-molecule formation in a Bose-Fermi mixture. Phys Rev A 2013;87:012703.
[17] Deh B, Gunton W, Klappauf BG, Li Z, Semczuk M, Van Dongen J, Madison KW. Giant Feshbach resonances in ^{6}Li-^{85}Rb mixtures. Phys Rev A 2010;82:020701.
[18] Tung S-K, Parker C, Johansen J, Chin C, Wang Y, Julienne PS. Ultracold mixtures of atomic ^{6}Li and ^{133}Cs with tunable interactions. Phys Rev A 2013;87:010702.
[19] Park JW, Wu C-H, Santiago I, Tiecke TG, Will S, Ahmadi P, Zwierlein MW. Quantum degenerate Bose-Fermi mixture of chemically different atomic species with widely tunable interactions. Phys Rev A 2012;85:051602.
[20] Wu C-H, Santiago I, Park JW, Ahmadi P, Zwierlein MW. Strongly interacting isotopic Bose-Fermi mixture immersed in a Fermi sea. Phys Rev A 2011;84:011601.
[21] Lin Y-J, Jiménez-García K, Spielman IB. Spin–orbit-coupled Bose–Einstein condensates. Nature 2011;471.
[22] Galitski V, Spielman IB. Spin–orbit coupling in quantum gases. Nature 2013;494(8):49–54.
[23] Wu Z, Zhang L, Sun W, Xu X-T, Wang B-Z, Ji S-C, Deng Y, Chen S, Liu X-J, Pan J-W. Realization of two-dimensional spin-orbit coupling for Bose-Einstein condensates. Science 2016;354(6308):83–8.
[24] Kartashov YV, Konotop VV, Abdullaev FK. Gap solitons in a spin-orbit-coupled Bose-Einstein condensate. Phys Rev Lett 2013;111:060402.
[25] Zezyulin DA, Driben R, Konotop VV, Malomed BA. Nonlinear modes in binary bosonic condensates with pseudo–spin-orbital coupling. Phys Rev A 2013;88:013607.
[26] Sakaguchi H, Li B, Malomed BA. Creation of two-dimensional composite solitons in spin-orbit-coupled self-attractive Bose-Einstein condensates in free space. Phys Rev E 2014;89:032920.
[27] Zhai H. Degenerate quantum gases with spin–orbit coupling: a review. Rep Progr Phys 2015;78(2):026001.
[28] Sakaguchi H, Malomed BA. One- and two-dimensional solitons in -symmetric systems emulating spin–orbit coupling. New J Phys 2016;18(10):105005.
[29] Sakaguchi H, Sherman EY, Malomed BA. Vortex solitons in two-dimensional spin-orbit coupled Bose-Einstein condensates: Effects of the Rashba-Dresselhaus coupling and Zeeman splitting. Phys Rev E 2016;94:032202.
[30] Li Y, Liu Y, Fan Z, Pang W, Fu S, Malomed BA. Two-dimensional dipolar gap solitons in free space with spin-orbit coupling. Phys Rev A 2017;95:063613.
[31] Li Y, Luo Z, Liu Y, Chen Z, Huang C, Fu S, Tan H, Malomed BA. Two-dimensional solitons and quantum droplets supported by competing self- and cross-interactions in spin-orbit-coupled condensates. New J Phys 2017;19(11):113043.
[32] Malomed BA. Creating solitons by means of spin-orbit coupling. Europhys Lett 2018;122(3):36001.
[33] Sowinski T, Garcia-March MA. One-dimensional mixtures of several ultracold atoms: a review. Rep Progr Phys 2019;82(10):104401.
[34] Ibrahim RA. Oscillons, walking droplets, and skipping stones (an overview). Nonlinear Dynam 2021;104(3):1829–88.
[35] Malomed B. Multidimensional solitons. AIP Publishing; 2022.
[36] Sakaguchi H, Malomed BA. One- and two-dimensional gap solitons in spin-orbit-coupled systems with Zeeman splitting. Phys Rev A 2018;97:013607.
[37] Kartashov YV, Torner L, Modugno M, Sherman EY, Malomed BA, Konotop VV. Multidimensional hybrid Bose-Einstein condensates stabilized by lower-dimensional spin-orbit coupling. Phys Rev Res 2020;2:013036.
[38] Wang P, Yu Z-Q, Fu Z, Miao J, Huang L, Chai S, Zhai H, Zhang J. Spin-orbit coupled degenerate Fermi gases. Phys Rev Lett 2012;109:095301.
[39] Cheuk LW, Sommer AT, Hadzibabic Z, Yefsah T, Bakr WS, Zwierlein MW. Spin-injection spectroscopy of a spin-orbit coupled Fermi gas. Phys Rev Lett 2012;109:095302.
[40] Adhikari SK, Malomed BA. Tightly bound gap solitons in a Fermi gas. Europhys Lett 2007;79(5):50003.
[41] Díaz P, Laroze D, Ávila A, Malomed BA. Two-dimensional composite solitons in a spin-orbit-coupled fermi gas in free space. Commun Nonlinear Sci Numer Simul 2019;70:372–83.
[42] Malomed BA. (INVITED) Vortex solitons: Old results and new perspectives. Physica D 2019;399:108–37.
[43] Díaz P, Pérez L, Reyes L, Laroze D, Bragard J. Taming Faraday waves in binary fermionic clouds: The effect of Zeeman interaction. Chaos Solitons Fractals 2021;153:111416.
[44] Fuchs JN, Recati A, Zwerger W. Exactly solvable model of the BCS-BEC crossover. Phys Rev Lett 2004;93:090408.
[45] Das KK. Bose-Fermi mixtures in one dimension. Phys Rev Lett 2003;90:170403.
[46] Salasnich L. Ideal quantum gases in D-dimensional space and power-law potentials. J Math Phys 2000;41(12):8016–24.
[47] Salasnich L, Pozzi B, Parola A, Reatto L. Thermodynamics of multi-component Fermi vapours. J Phys B: At Mol Opt Phys 2000;33(19):3943.
[48] Adhikari SK. Free expansion of fermionic dark solitons in a boson–fermion mixture. J Phys B: At Mol Opt Phys 2005;38(19):3607.
[49] Adhikari SK. Mixing-demixing in a trapped degenerate fermion-fermion mixture. Phys Rev A 2006;73:043619.
[50] Adhikari SK. Superfluid Fermi-Fermi mixture: Phase diagram, stability, and soliton formation. Phys Rev A 2007;76:053609.
[51] Adhikari SK, Malomed BA. Miscibility in a degenerate fermionic mixture induced by linear coupling. Phys Rev A 2006;74:053620.
[52] Salasnich L, Adhikari SK, Toigo F. Self-bound droplet of Bose and Fermi atoms in one dimension: Collective properties in mean-field and Tonks-Girardeau regimes. Phys Rev A 2007;75:023616.
[53] Adhikari SK, Salasnich L. One-dimensional superfluid Bose-Fermi mixture: Mixing, demixing, and bright solitons. Phys Rev A 2007;76:023612.
[54] Díaz P, Laroze D, Schmidt I, Malomed BA. One- and two-dimensional reductions of the mean-field description of degenerate Fermi gases. J Phys B: At Mol Opt Phys 2012;45(14):145304.
[55] Díaz P, Laroze D, Malomed BA. Correlations and synchronization in a Bose–Fermi mixture. J Phys B: At Mol Opt Phys 2015;48(7):075301.
[56] Bychkov YA, Rashba EI. Oscillatory effects and the magnetic susceptibility of carriers in inversion layers. J Phys C: Solid State Phys 1984;17(33):6039.
[57] Bogoliubov NN, Shirkov DV. Introduction to the theory of quantized fields. 1973.
[58] Press W. Numerical recipes 3rd edition: The art of scientific computing. Numerical recipes: The art of scientific computing, Cambridge University Press; 2007.
[59] Bergé L. Wave collapse in physics: principles and applications to light and plasma waves. Phys Rep 1998;303(5):259–370.
[60] Vakhitov NG, Kolokolov AA. Stationary solutions of the wave equation in a medium with nonlinearity saturation. Radiophys Quantum Electron 1973;16:783–9.
[61] Sakaguchi H, Malomed BA. Solitons in combined linear and nonlinear lattice potentials. Phys Rev A 2010;81:013624.
[62] Dong L, Fan M, Malomed BA. Stable higher-charge vortex solitons in the cubic–quintic medium with a ring potential. Opt Lett 2023;48(18):4817–20.